# Statistical analyzing the effect of ionospheric irregularity on GNSS radio occultation atmospheric measurement

Mingzhe Li [1,2,3,4], Xinan Yue [1,2,3,4]

[1] Key Laboratory of Earth and Planetary Physics, Institute of Geology and Geophysics, Chinese Academy of Sciences, Beijing, China

[2] Innovation Academy for Earth Science, CAS, Beijing, China

[3] Beijing National Observatory of Space Environment, Institute of Geology and Geophysics, Chinese Academy of Sciences, Beijing, China

[4] College of Earth and Planetary Sciences, University of Chinese Academy of Sciences, Beijing, China

*Correspondence to*: Xinan Yue (yuexinan@mail.iggcas.ac.cn)

**Abstract**. The Global Navigation Satellite System (GNSS) atmospheric radio occultation (RO) has been an effective method for Earth's atmosphere exploring. RO signals propagate through ionosphere before reaching the neutral atmosphere. The GNSS signal is affected by the ionospheric irregularity including the sporadic E (Es) and the F region irregularity due to mainly multipath effect. The effect of ionospheric irregularity on atmospheric RO data has been demonstrated by several studies in terms of cases. However, its statistical effect has not been investigated comprehensively. In this study, based on the Constellation Observing System for Meteorology, Ionosphere, and Climate (COSMIC) RO data during 2011-2013, the failed inverted RO events occurrence rate and the bending angle oscillation, which is defined as the standard deviation of the bias between the observed bending angle and the National Center for Atmospheric Research (NCAR) climatology model bending angle between 60 and 80 km, were used for statistical analysis. It is found that in middle and low latitudes during the daytime, the failed inverted RO occurrence and the bending angle oscillation show obvious latitude, longitude, and local time variations, which correspond well with the Es occurrence features. The F region irregularity (FI) contributes to the obvious increase of the failed inverted RO occurrence rate and the bending angle oscillation value during the nighttime over the geomagnetic equatorial regions. For high latitude regions, the Es can increase the failed inverted RO occurrence rate and the bending angle oscillation value during the nighttime. There also exists the seasonal dependency of the failed inverted RO event and the bending angle oscillation. Overall, the ionospheric irregularity effects on GNSS atmospheric RO measurement

exist in terms of failed RO event inversion and bending angle oscillation statistically. Awareness of these effects could benefit both the data retrieval and applications of RO in the lower atmosphere.

## 1. Introduction

The radio occultation (RO) is a technique originally developed in the late 1960s and early 1970s for planetary atmosphere exploring. With the great development of the Global Navigation Satellite System (GNSS) over the past 30 years, the GNSS signal has been an effective source for exploring the Earth's atmosphere. Several RO missions such as the Global Positioning System Meteorology (GPS/MET), the Challenging Minisatellite Payload (CHAMP) (Wickert et al., 2001), the Scientific Application Satellite-C (SAC-C), the Gravity Recovery and Climate Experiment (GRACE) (Beyerle et al., 2005), the Constellation Observing System for Meteorology, Ionosphere and Climate (COSMIC) (Schreiner et al., 2007), the Meteorological Operational Satellite Program (Metop) A/B, the Fengyun-3C (FY-3C) (Mao et al., 2016) and et al have proven the good capability of RO for observing the Earth's ionosphere and atmosphere. High-quality products of RO have been used for space weather, weather and climate research (Anthes et al., 2008).

The RO technique could be divided into the ionospheric RO and the atmospheric RO. For the former one, the GNSS signal propagates through the ionosphere. Dual-frequency pseudo-range and carrier phase can be observed by the receiver onboard the low Earth orbit (LEO) satellite and be used to invert the electron density profile. Besides, the amplitude and phase measurements can be used to calculate the ionospheric scintillation index such as the S4 index. The S4 index is defined as the standard deviation of the received signal power normalized to the average signal power, it can represent the occurrence of the ionospheric irregularity (Yue et al., 2016). ~~Besides, the amplitude and phase measurements can be used to calculate the ionospheric scintillation index such as the S4 index, which can represent the occurrence of the ionospheric irregularity (Yue et al., 2016)~~. For the latter one, the GNSS signal propagates through both the ionosphere and the neutral atmosphere. The dual-frequency carrier phase can be used to calculate the bending angle and then invert the atmospheric parameters. As a result, the effects on signals caused by the ionosphere should be removed before deriving the atmospheric RO products.

59    For atmospheric RO, the GNSS signal is mainly affected by the ionosphere in two ways. Firstly, the

60    existence of dense ionospheric electron density contributes to the bending of signals. Similar to the first-

61    order ionospheric term calibration used in ground-based dual-frequency observations, a linear

62    combination of the two-band signal bending at the same impact parameter is usually used to remove the

63    ionospheric effect (Vorob'ev and Krasil'nikova, 1994). However, after the linear combination of bending

64    angles, there still exists a residual ionospheric error (RIE). The RIE could bring ionospheric variability

65    such as solar cycle, local time, and seasonal variations into atmospheric RO products although its

66    amplitude is relatively low (Li et al., 2020). It means that the climate research using atmospheric RO

67    products would be affected by the ionosphere. Some efforts have been tried for the RIE calibration

68    (Danzer et al., 2013, 2015, 2020; Healy and Culverwell, 2015; Angling et al. 2018; Liu et al., 2018, 2020;

69    Li et al., 2020). Danzer et al. (2013) have analyzed the bending angle bias of CHAMP and COSMIC RO

70    data from 2001-2011 and tried to parameterize bending angle bias versus the solar cycle to make

71    statistical corrections. Healy and Culverwell (2015) found a good correlation between the RIE and the

72    difference of GPS L1 and L2 bending angles at the same impact parameter. They then proposed a

73    correction method using the 'kappa' parameter under the ionospheric spherical symmetry assumption.

74    This method was further tested by Danzer et al. (2015), Angling et al. (2018) and Danzer et al. (2020). It

75    can reduce the systematic errors vary with solar cycle from 0.2 K to 2.0 K at altitudes between 40 km to

76    45 km. Liu et al. (2018) have analyzed the ionospheric structure influences on RIE in bending angles

77    based on ray tracing simulations and further developed a "Bi-local correction approach" to calculate the

78    RIE through an equation. This method considers both the ionospheric asymmetry effects as well as the

79    geomagnetic effects on bending angles (Liu et al., 2020). In our previous study, we have also

80    characterized the RIEthis effects statistically by both ray-tracing simulation and data analysis (Li et al.,

81    2020). Secondly, the small-scale irregularities in the ionosphere also have an impact on the GNSS signal

82    and finally affect the atmospheric RO products. The small-scale irregularities of which interest to this

83    study are the sporadic E (Es) and the F region irregularity (FI). As indicated by former studies, the

84    ionospheric irregularity will cause refraction or diffraction of the GNSS signal during its propagating

85    through the ionosphere. The received signals could show temporal fluctuations in both amplitude and

86    phase, which is known as the ionospheric scintillation. The impact of the small-scale irregularity on

87    atmospheric RO can be significant but show quite different climatologically characteristics in

88    comparison with the large-scale ionospheric effects (Li et al., 2020). Besides, it is difficult to model the

89    ionospheric irregularity in a deterministic fashion for simulation research (Mannucci, et al., 2011).

90    Previous studies only pointed out this small scale ionospheric effect in terms of cases (Zeng and

91    Sokolovskiy, 2010). To our knowledge, there is no comprehensive study giving statistical analysis

92    between ionospheric irregularity and atmospheric RO products, which is quite important to quantify this

93    effect and therefore benefit atmospheric RO data retrieval and application. This is the main objective of

94    this study.

95

96    In the following sections, we try to study the ionospheric irregularity effects on GNSS atmospheric RO

97    measurement statistically. Based on previous related studies, the current study will make sense as

98    following advantages: (1) the correlation between failed inverted COSMIC RO events and the

99    ionospheric irregularity are analyzed; (2) morphology of the bending angle oscillation in the atmospheric

100   RO measurement are presented in comparison with the occurrence rate of both Es and FI; (3) the seasonal

101   dependency of failed inverted RO events and the bending angle oscillation is analyzed. We will describe

102   the COSMIC observation and the statistical method in Section 2 and Section 3, respectively. Then the

103   ionospheric irregularity effects on single RO cases will be shown in Section 4. The statistical results of

104   the failed inverted RO event and the bending angle oscillation will be depicted in comparison with the

105   ionospheric irregularity occurrence rate in Section 5. Finally, the conclusions and implications will be

106   presented in Section 6.

107

108   **2.  RO Data Description**

109   COSMIC, as one of the most successful RO missions, was launched on 15 April 2006. The constellation

110   with six LEO satellites has contributed millions of profiles for space weather, weather, and climate

111   research in the past 14 years. Each COSMIC satellite has four separate antennas: two high gain

112   occultation antennas received GNSS signals with a 50 Hz sampling rate to explore the neutral atmosphere

113   from the top (~130 km) to bottom or reverse. The carrier phase modulated on signals can be used for

114   excess phase calculating and atmospheric parameters retrieving. The other two antennas are precise orbit

115   determination (POD) antennas with a 1 Hz sampling rate. The received signals are used for LEO orbiting,

116   ionosphere electron density, slant total electron content (TEC), and scintillation index calculating

117     (Schreiner et al., 2007, 2011). The COSMIC data are processed by the COSMIC Data Analysis and

118     Archive Center (CDAAC) of the University Corporation for Atmospheric Research (UCAR) and

119     available on the CDAAC website (http://cdaac-www.cosmic.ucar.edu/). In this study, the COSMIC RO

120     observations during 2011-2013 were used for analysis. The S4 scintillation index in auxiliary data file

121     (scnLv1) was used for the Es and FI occurrence rates calculation. The dry atmospheric profiles file

122     (atmPrf) were used for the failed inverted RO occurrence rate calculation and the atmospheric bending

123     angle oscillation morphology analysis. The specific calculating method will be introduced in the

124     following section.

125

126     **3.    Analysis Method**

127     To study the ionospheric irregularity effects on RO, we focus on analyzing two parameters: the failed

128     inverted RO event occurrence rate and the bending angle oscillation defined as the mean standard

129     deviation of the bias between the observed bending angle and the NCAR climatology model bending

130     angle during the 60-80 km altitude interval. The failed inverted RO event means those events flunked

131     the quality control during profiles inversion in CDAAC. They are identified by the 'bad' attribute in the

132     atmPrf file whose values are equal to 1. The oscillation of atmospheric RO bending angle is also provided

133     by the atmPrf file. The S4 index contained in the scnLv1 file is used to represent the occurrence of the

134     ionospheric irregularity. The occurrence rate of S4 index larger than 0.3 is set to represent the occurrence

135     of ionospheric irregularity. It should be noted that we identify the occurrence altitude range between

136     50~600 km as the contribution of both Es and FI together. We first calculated the failed inverted RO

137     event occurrence rate in comparison with the ionospheric irregularity occurrence rate. After that, failed

138     inverted RO events of COSMIC during 2011-2013 were screened out to study the Es and FI effects on

139     the bending angle observation. Additionally, the ionPrf file of CDAAC is used for displaying the electron

140     density profiles in single cases.

141

142     **4.    Ionospheric Irregularity Effect on Single RO Cases**

143     To have a preliminary knowledge of the ionospheric irregularity effect on atmospheric RO, we firstly

144     show several typical single case examples. The results are shown in Figure 1. From top to bottom, each

145     row show results of a case. The three cases represent the RO event without ionospheric irregularity, the

RO event affected by the Es, and the event affected by the FI, respectively. From left to right columns, the panels represent the inverted bending angles, the signal-to-noise ratio (SNR) of L1 C/A signal, the related electron density profile, and the inverted dry temperature profile compared with the European Centre for Medium-Range Weather Forecasts (ECMWF) results. Please note that the grey lines in the rightmost panels denote the results of RO inverted temperature and the red lines represent those of ECMWF. The purple lines in case 1 and case 3 are the temperature bias multiplied by 10 for convenient comparison. The features of L1 C/A SNR profile and the electron density profile could identify whether a RO event is affected by the ionospheric irregularity (Yue et al., 2015). As depicted in the second column, the case 2 shows visible peaks in SNR fluctuation around 110 km, which correspond to the occurrence altitude range of Es and could reflect the Es effects on this event. Besides, the electron density profile of case 3 shows obvious scintillation between 200 km and 300 km, which implies the FI impact on signals. We also use the corresponding CDAAC scnLv1 file for verification. The S4 maximum values of cases 1-3 are 0.03, 0.59, and 1.21, with S4 peaks around 111.69, 108.45, and 274.86 km, respectively. It can be seen that the normal case shows good inversion results. The value of the ionospheric-corrected LCLC bending angle above 40 km is much smaller than those of the L1 and L2 bending angles. It means that the ionosphere dominates the bending of the RO signal in this tangent altitude interval and the linear combination method works well. The bias between the observed dry temperature and the ECMWF result is insignificant. However, the Es case shows bad results. Values of the inverted L2 bending angle are negative, which leads to larger values of LC bending angle after the linear combination. As a result, the temperature profile is failed inverted. Significant temperature bias between the observation and model result can be seen from the rightmost panel. For the FI case, oscillations can be seen in the LC bending angle profile in the leftmost panel as well as the temperature bias profile in the rightmost panel. The bending angle oscillation values of cases 1-3 are 0.66, 16.06, and 5.74 μrad, respectively. It indicates that this oscillation could also be related to the ionospheric irregularity. The geometry of atmospheric RO observation determines that the ionospheric irregularity effects could propagate to a deep tangent height, where far below the altitude range of irregularity occurrence (Wu, 2020). We have gone through many cases and found that the failed inverted RO event and strong bending angle oscillation occurs usually along with Es and FI occurrence. But not all events affected by the Es and FI are failed inverted. The analysis of single cases motivates our further statistical study.

6

175

## 5. Statistical Results

177 The Es and FI have been investigated comprehensively in the past several decades (Hocke et al., 2001;

178 Straus et al., 2003; Wu, 2005; Arras et al., 2008, 2009; Carter et al., 2013; Yue et al., 2015, 2016).

179 Generally, the Es can be seen as thin layers with much higher plasma density than the normal E region

180 density occurring during the altitude range of ~ 90-120 km. The occurrence rate of Es is controlled by

181 many factors such as the tidal wind, the Earth's geomagnetic field, and metal ions (Axford, 1963; Chu et

182 al., 2014). These factors lead to the complicate variations of Es along with latitude, longitude, altitude,

183 local time, and season (Hocke et al., 2001; Wu, 2005; Arras et al., 2008, 2009). FI is the plasma

184 irregularity and inhomogeneity in the F region caused by plasma instabilities (Dungey, 1956; Fejer and

185 Kelley, 1980). The scale sizes of the density irregularity range from a few centimeters to hundreds of

186 kilometers and the irregularity can appear at all latitudes. Both Es and FI have been observed by

187 ionosonde, incoherent/coherent scatter radars, and ground-based GNSS network. Since the success of

188 GPS/MET, the GNSS RO has also been proven as an effective technique to detect the occurrence of Es

189 and FI. Hocke et al. (2001) first derived the occurrence of Es from the GPS/MET observation and

190 confirmed its seasonal variation. Wu (2005) studied the latitude, local time, altitude, and seasonal

191 dependency of Es by using CHAMP occultation data. Arras et al. (2008) further investigated the

192 occurrence of Es using multiple RO missions including CHAMP, GRACE-A, and COSMIC. Chu et al.

193 (2014) presented the morphology of Es based on COSMIC amplitude and phase fluctuations of L-band

194 signals. For FI, Straus et al. (2003) made a statistical analysis of the GPS C/A code SNR fluctuations on

195 L1 frequency based on observations onboard the PICOSat satellite. They found that the geographic and

196 local time distributions of occultation having large values of the S4 index were consistent with known

197 scintillation climatology. Brahmanandam et al. (2012) presented the three-dimensional global

198 morphology and seasonal variations of S4 index measured from COSMIC for a low solar activity year

199 2008 and found the latitude, altitude, and local time dependency of FI. Carter et al. (2013) further

200 revealed the longitudinal and seasonal variations of equatorial FI using COSMIC S4 index. Besides, Yue

201 et al. (2015, 2016) also studied the complex Es and the ionospheric irregularity related GPS RO loss of

202 lock by COSMIC S4 index.

203

204 As investigated in the single case section, the failed inverted RO event and bending angle oscillation

205 could be related to the ionospheric irregularity. So we carried out statistical research from all COSMIC

206 atmospheric events during 2011-2013. Firstly, the RO event whose 'bad' attribute in the atmPrf file equals

207 to 1 was selected as the failed inverted RO for the statistics. Then the failed inverted RO events were

208 screened out for the bending angle oscillation study. Both tThe geographical and geomagnetic

209 distributions of Es and FI are plotted separately in Figure 2. The mixed Es and FI occurrence rateof the

210 ionospheric irregularity, the failed inverted RO event occurrence rate and the bending angle oscillation

211 are shown in Figure 23. The grid resolutions are 10° ×3° for Lon×Lat and 3° ×2 h for MLat×MLT,

212 respectively.

213

214 As depicted in Figure 3, tThe global geographical distribution of both Es and FI occurrence rate together

215 is depicted in the top left panel. For low and middle latitudes, two peaks of Es occurrence rate locate in

216 the East Asia region and the North Africa region in the northern hemisphere. One peak locates near the

217 South America region. The values of occurrence rate are greater than 30% in peak regions. One trough

218 can be seen around the South Africa region with an occurrence rate lower than 10%. The result

219 corresponds well with the Es characteristics derived from the GPS RO phase and SNR fluctuations (Wu,

220 2005). Besides, an occurrence enhancement can be seen around the West Africa and the Atlantic Ocean

221 region, which agrees with the previous studies base on COSMIC S4 index (Brahmanandam et al., 2012;

222 Yue et al., 2016) and indicates the contributions of FI. For high latitudes, two peaks are available during

223 120° W-150° W and 0°-60° E in the northern hemisphere and one peak can be seen around 120° E near

224 North Antarctica. In the top middle panel, we plotted the occurrence rate of failed inverted RO events

225 during 2011-2013. The rate represents the failed inverted RO event in percentage which was calculated

226 based on all observed COSMIC RO events during this time interval. Overall, the global distribution of

227 the failed inverted RO event occurrence agrees with those of the Es occurrence in the top left panel. Two

228 peaks in the northern hemisphere and one in the southern hemisphere match the locations of Es

229 occurrence peaks around ±20°. Besides, there exists an obvious increase in the failed inverted RO events

230 in high latitudes. It should be noted that the occurrence rate distribution of failed inverted RO event can't

231 match those of Es and FI completely because the inversion error is not only affected by the ionospheric

232 irregularity but also affected by other factors such as the low SNR. However, the contribution of FI on

233    the failed inverted RO event is not obvious in this panel. This might be due to the high occurrence regions

234    of FI overlaps those of Es partly. In the top right panel, we plotted the global distributions of the median

235    bending angle oscillation. The results are also in good agreement with those patterns of Es and FI

236    occurrence rate. Strong oscillations can be seen around North Africa and the East Asia regions in the

237    Northern Hemisphere and around South America in the Southern Hemisphere, with bending angle

238    oscillation values of ~1.4 μrad. The trough of bending angle oscillation can be seen around the South

239    Africa regions with values less than 1 μrad. Both the locations of peaks and troughs correspond well

240    with those of Es occurrence rate. Besides, larger oscillation values are available in the Atlantic Ocean

241    around the equator, which could be related to the high FI occurrence in these regions. Especially, both

242    the failed inverted RO and the bending angle oscillation show obvious peaks around 120° E near North

243    Antarctica. Peaks of the two parameters could be related to the high occurrence of both Es and FI in this

244    region. Peaks of Es and FI occurrence in this region have also been observed by Wu (2020) based on S4

245    index from RO data sets.

246

247    We also plotted the geomagnetic local time and latitude (MLT-MLat) distribution of the three parameters

248    in the bottom panels in Figure 2 3 for further comparison. In most regions of the bottom left panel, the

249    distributions are similar to those of the Es. Irregularity occurs more around geomagnetic equator regions

250    and the aurora oval regions. Around the geomagnetic equator regions during 18-24 MLT, there is an

251    occurrence enhancement caused by FI. Both Es and FI contributes to a 'three peaks' feature in the equator

252    regions after sunset. These features correspond to the previous studies observed no matter by ground-

253    based GNSS observations (Li et al., 2011) or COSMIC RO observations (Chen and Huang, 2017).

254    Similar features can be seen in the bottom middle panel. The occurrence rate of the failed inverted RO

255    event is higher around the equator regions from sunset to midnight, which can reach 20%. In high

256    latitudes, two ovals are available. Besides, the failed inverted RO event also occurs more after midnight

257    and during the noon in the Southern Hemisphere. In these regions, the FI could make contributions. For

258    bending angle oscillation in the bottom right panel, three peaks of the mean oscillation value exist along

259    the geomagnetic latitude, which denotes the contribution of Es and FI during the nighttime. The value of

260    bending angle oscillation tends to be small within ±60° during 2~10 MLT. For high latitudes, the

261    bending angle shows strong oscillation even though the occurrence rate of Es and FI is lower than those

262  of peak regions in middle and low latitudes.

263

264  For a better display of the high-latitude results, we plotted the irregularity and failed inverted RO

265  occurrence rates as well as the bending angle oscillation variation with MLT-MLat in northern and

266  southern polar regions in Figure 34. As depicted in the left two panels, the ionospheric irregularity mainly

267  occurs during 18-24 MLT, with occurrence peaks existing in aurora regions around midnight and moving

268  toward the polar cap regions when approaching the sunset time. Values of the irregularity occurrence rate

269  are around 10-20% during the nighttime and can reach 30% for peak regions. The middle two panels

270  show the occurrence rate of failed inverted RO events. It is depicted that the peaks are located in aurora

271  regions and extent to the polar cap regions from sunset time to midnight. The increase in the occurrence

272  rate around these regions might be affected by the high occurrence rate of Es. The failed inverted RO

273  occurrence rates are also higher during the daytime in both hemispheres although the irregularity

274  occurrence rates are lower than 10% during this period. The right panels show the bending angle

275  oscillation results. Its value is larger in aurora regions around midnight, which can reach 2.1 μrad. For

276  those values in the South Hemisphere, strong bending angle oscillation can be seen in the polar cap

277  regions no matter during the daytime or nighttime. Besides, the peak regions locate mainly between

278  80° S-90° S instead of the 70° S-80° S as the irregularity occurrence peak shown in the bottom middle

279  panel.

280

281  We also use the scatter plot to study correlations between the ionospheric irregularity and the two

282  parameters. The results were plotted in Figure 45. Considering patterns of the failed inverted RO

283  occurrence rate and the bending angle oscillation could not agree very well with those of the irregularity

284  in high latitude regions, we mainly pay attention to the results in low and middle latitudes (60° S-60° N).

285  Correlations during the daytime (6~18 MLT) and the nighttime (0~6, 18~24 MLT) were displayed

286  respectively. Overall, the correlations between the ionospheric irregularity and the two parameters are

287  significant although they are not strictly liner especially for the bending angle oscillation during the

288  daytime. The scatters in the panels are probably due to that the bending angle oscillation is not only

289  affected by the Es and FI but also related to other factors. Meanwhile, the observation and inversion noise

290  could also make contributions.

291

292   In Figures 23-45, we mainly concern about the yearly average pattern. As stated above, the seasonal

293   variation of irregularity has been confirmed by previous studies (Arras et al., 2008; Chen and Huang,

294   2017). So the seasonal dependency of the failed inverted RO event and the bending angle oscillation

295   could also exist. For further investigating, the occurrence rate variation with Lon-Lat and MLT-MLat

296   were depicted in Figure 5-6 and Figure 67, respectively. Equinox (March, April, September, and October),

297   Northern Summer (May, June, July, and August), and Northern Winter (January, February, November,

298   and December) are considered here. Generally, in Figure 56, the distributions of the failed inverted RO

299   event occurrence are in good agreement with those of the irregularity. Both parameters are larger within

300   ±30° in Equinox and larger in summer than in winter. For Northern Summer, the occurrence peaks are

301   near the North Africa area and the East Asia area. For Northern Winter, the peaks are available in the

302   Pacific Ocean regions nearby South America. Similar to the average pattern in Figure 23, the failed

303   inverted RO occurrence rate is high in polar regions even though the Es and FI occurrence is not obvious

304   in comparison with those of peak regions in low latitudes. The MLT-MLat distributions of the irregularity

305   and the failed inverted RO in Figure 6-7 also show similar seasonal variations. But for the southern polar

306   region in Equinox and the northern polar region in Northern Winter, the failed inverted RO occurs

307   significantly on condition that the occurrences of Es and FI are not obvious. This might be due to that

308   the FI occurrence is lower than those of Es in high latitudes but it plays the main role in the failed inverted

309   RO occurrence in these months. For the bending angle results in both bottom panels in Figures 5-6 and

310   67, it is apparent that the bending angle oscillation value also follows a similar seasonal variation with

311   the ionospheric irregularity occurrence, which is larger in summer than in winter with the equinox as the

312   transitory season. It is noticeable that for the geographic distribution, larger values exist around Northern

313   Antarctica in all seasons. For the geomagnetic distributions, the three peaks along geomagnetic latitudes

314   are available in all seasons.

315

316   **6.   Conclusions and Implications**

317   In this paper, we focus on the ionospheric irregularity effects on GNSS atmospheric RO. The failed

318   inverted RO events and the bending angle oscillation are the two main parameters we concerned about.

319   The COSMIC S4 index provided by CDAAC during 2011-2013 is used to characterize the ionospheric

320   irregularity occurrence rate such as the Es and the F region irregularity. The 'bad' attribute in the atmPrf

321   file is used to identify the failed inverted RO events on condition that its value equals to 1. The mean

322   bending angle oscillation also from the atmPrf file is used to reflect the degree of bending angle

323   oscillation. Results from single cases are analyzed firstly. Then the distribution patterns and seasonal

324   variations of the ionospheric irregularity occurrence rate, failed inverted RO event occurrence rate, and

325   the bending angle oscillation are presented for the correlation study. The main conclusions and

326   implications of the paper are summarized in the following:

327   (1)  The ionospheric irregularity such as the Es and the F region irregularity could affect the GNSS

328       atmospheric RO in terms of causing failed inverted RO events and the bending angle oscillation in

329       both cases and statistically.

330   (2)  In middle and low latitudes, during the daytime, both the failed inverted RO event and the bending

331       angle oscillation are mainly affected by the Es. During the nighttime, the F region irregularity

332       contributes to the obvious increases of the failed inverted RO occurrence rate and the bending angle

333       oscillation around the geomagnetic equatorial regions.

334   (3)  In the polar regions, the Es mainly affect the two parameters in the aurora regions from sunset to

335       midnight. But the correlations between the ionospheric irregularity and the two parameters are not

336       as obvious as those in middle and low latitudes.

337   (4)  Seasonal dependency of the failed inverted RO occurrence and the bending angle oscillation exists,

338       which also accord well with the seasonal variation of the Es and the F region irregularity.

339   (5)  The occurrence rate of the failed inverted RO can reach 15% in low latitudes and even 20% in peak

340       regions. It means that hundreds of COSMIC RO events per day will be ruled out during quality

341       control. The bending angle oscillation between 60 and 80 km also varies from ~0.6 $\mu$rad in trough

342       regions to ~2.5 $\mu$rad in peak regions. Although 60~80 km is not the main altitude range of RO data,

343       the small-scale effects in atmospheric RO exist in all altitudes and could affect the atmospheric

344       research related to RO products. Awareness of the ionospheric irregularity effect on RO could be

345       beneficial to improve the data retrieval, quality control of GNSS atmospheric RO data processing

346       and data assimilation application in numerical weather prediction (Cardinali and Healy, 2014).

347   Overall, the ionospheric irregularity effects on GNSS atmospheric RO measurement exist in terms of

failed RO event inversion and bending angle oscillation statistically. It makes the calibration of ionospheric irregularity effects on RO more challenging and urgent. A suitable filter may be helpful in reducing the ionospheric irregularity effects on bending angles and including ruled-out events in the processing. The potential method needs to be more investigated and we hope to study it in our further work. Besides, the causing of failed inverted RO events in high latitudes is also needed to be studied.

**8. References**

Axford, W. I.: The formation and vertical movement of dense ionized layers in the ionosphere due to neutral wind shears, Journal of Geophysical Research, 68, 769–779, doi:10.1029/JZ068i003p00769, 1963.

Anthes, R. A., Bernhardt, P. A., Chen, Y., Cucurull, L., Dymond, K. F., Ector, D., Healy, S. B., Ho, S. P., Hunt, D. C., Kuo, Y. H., Liu, H., Manning, K., McCormick, C., Meehan, T. K., Randel, W. J., Rocken, C., Schreiner, W. S., Sokolovskiy, S. V., Syndergaard, S., Thompson, D. C., Trenberth, K. E., Wee, T. K., Yen, N. L., and Zeng, Z.: The COSMIC/FORMOSAT-3 mission: Early results, Bulletin of the American Meteorological Society, 89, 313–333, doi.org/10.1175/BAMS-89-3-313, 2008.

Angling, M. J., Elvidge, S., and Healy, S. B.: Improved model for correcting the ionospheric impact on bending angle in radio occultation measurements, Atmospheric Measurement Techniques, 11, 2213-2224, doi.org/10.5194/amt-11-2213-2018, 2018.

376  Arras, C., Wickert, J., Beyerle, G., Heise, S., Schmidt, T., and Jacobi, C.: A global climatology of

377  ionospheric irregularities derived from GPS radio occultation, Geophysical Research Letters, 35,

378  doi:10.1029/2008gl034158, 2008.

379  Arras, C., Jacobi, C., and Wickert, J.: Semidiurnal tidal signature in sporadic E occurrence rates derived

380  from GPS radio occultation measurements at higher midlatitudes, Ann Geophys, 27, 2555–2563, 2009.

381  Beyerle, G., Schmidt, T., Michalak, G., Heise, S., Wickert, J., and Reigber, C.: GPS radio occultation

382  with GRACE: Atmospheric profiling utilizing the zero difference technique, Geophysical Research

383  Letters, doi.org/10.1029/2005gl023109, 2005.

384  Brahmanandam, P. S., Uma, G., Liu, J. Y., Chu, Y. H., Latha Devi, N.S.M.P., and Kakinami, Y.: Global

385  S4 index variations observed using FORMOSAT-3/COSMIC GPS RO technique during a solar minimum

386  year, Journal of Geophysical Research: Space Physics, 117, doi:10.1029/2012ja017966, 2012.

387  Cardinali, C. and Healy, S.: Impact of GPS radio occultation measurements in the ECMWF system using

388  adjoint-based diagnostics, Quarterly Journal of the Royal Meteorological Society, 140, 2315-2320,

389  doi:10.1002/qj.2300, 2014.

390  Carter, B.A., Zhang, K., Norman, R., Kumar, V. V., and Kumar, S.: On the occurrence of equatorial F-

391  region irregularities during solar minimum using radio occultation measurements, Journal of

392  Geophysical Research: Space Physics, 118, 892-904, doi:10.1002/jgra.50089, 2013.

393  Chu, Y. H., Wang, C. Y., Wu, K. H., Chen, K. T., Tzeng, K. J., Su, C. L., Feng, W., and Plane, J. M. C.:

394  Morphology of sporadic E layer retrieved from COSMIC GPS radio occultation measurements: Wind

395  shear theory examination, Journal of Geophysical Research: Space Physics, 119, 2117-2136,

396  doi:10.1002/2013ja019437, 2014.

397  Chen, S. and Huang, Z.: Ionospheric F-layer global scintillation index variation using COSMIC during

398  the period of 2007–2013, GPS Solutions, 21, 1049-1058, doi:10.1007/s10291-016-0593-2, 2017.

399  Dungey, J. W.: Convective diffusion in the equatorial F region, Journal of Atmospheric and Terrestrial

400  Physics, 9, 304-310, doi.org/10.1016/0021-9169(56)90148-9, 1956.

401  Danzer, J., Scherllin-Pirscher, B., and Foelsche, U.: Systematic residual ionospheric errors in radio

402  occultation data and a potential way to minimize them, Atmospheric Measurement Techniques, 6, 2169-

2179, doi.org/10.5194/amt-6-2169-2013, 2013.

Danzer, J., Healy, S. B., and Culverwell, I. D.: A simulation study with a new residual ionospheric error model, for GPS radio occultation climatologies, Atmospheric Measurement Techniques, 8, 3395-3404, doi.org/10.5194/amt-8-3395-2015, 2015.

Danzer, J., Schwaerz, M., Kirchengast, G., and Healy, S. B.: Sensitivity analysis and impact of the kappa-correction of residual ionospheric biases on radio occultation climatologies, Earth and Space Science, 7, e2019EA000942, doi.org/10.1029/2019EA000942, 2020.

Fejer, B. G. and Kelley, M. C.: Ionospheric irregularities. Reviews of Geophysics, 18, 401–454, doi:10.1029/RG018i002p00401, 1980.

Hocke, K., Igarashi, K., Nakamura, M., Wilkinson, P., Wu, J., Pavelyev, A., and Wickert, J.: Global sounding of sporadic E layers by the GPS/MET radio occultation experiment, Journal of Atmospheric and Solar-Terrestrial Physics, 63, 1973–1980, 2001.

Healy, S. B., Culverwell, I. D.: A modification to the standard ionospheric correction method used in GPS radio occultation, Atmospheric Measurement Techniques, 8, 3385-3393, doi.org/10.5194/amt-8-3385-2015, 2015.

Li, G., Ning, B., Abdu, M. A., Yue, X., Liu, L., Wan, W., and Hu, L.: On the occurrence of postmidnight equatorial Fregion irregularities during the June solstice, Journal of Geophysical Research: Space Physics, 116, doi:10.1029/2010ja016056, 2011.

Liu, C., Kirchengast, G., Sun, Y., Zhang, K., Norman, R., Schwaerz, M., Bai, W., Du, Q., and Li, Y.: Analysis of ionospheric structure influences on residual ionospheric errors in GNSS radio occultation bending angles based on ray tracing simulations, Atmospheric Measurement Techniques, 11, 2427-2440, doi.org/10.5194/amt-11-2427-2018, 2018.

Liu, C., Kirchengast, G., Syndergaard, S., Schwaerz, M., Danzer, J., and Sun, Y.: New Higher-Order Correction of GNSS RO Bending Angles Accounting for Ionospheric Asymmetry: Evaluation of Performance and Added Value, Remote Sensing, 12, doi.org/10.3390/rs12213637, 2020.

Li, M., Yue, X., Wan, W., and Schreiner, W. S.: Characterizing Ionospheric Effect on GNSS Radio Occultation Atmospheric Bending Angle, Journal of Geophysical Research: Space Physics, 125,

430    doi.org/10.1029/2019JA027471, 2020.

431    Mannucci, A. J., Ao, C. O., Pi, X., and Iijima, B. A.: The impact of large scale ionospheric structure on

432    radio occultation retrievals, Atmospheric Measurement Techniques, 4, 2837-2850, doi.org/10.5194/amt-

433    4-2837-2011, 2011.

434    Mao, T., Sun, L., Yang, G., Yue, X., Yu, T., Huang, C., Zeng, Z., Wang, Y., and Wang, J.: First Ionospheric

435    Radio-Occultation Measurements From GNSS Occultation Sounder on the Chinese Feng-Yun 3C

436    Satellite, IEEE Transactions on Geoscience and Remote Sensing, 54, doi.org/1-10.

437    10.1109/TGRS.2016.2546978, 2016.

438    Straus, P. R., Anderson, P. C., and Danaher, J. E.: GPS occultation sensor observations of ionospheric

439    scintillation, Geophysical Research Letters, 30, doi:10.1029/2002gl016503, 2003.

440    Schreiner, W., Rocken, C., Sokolovskiy, S., Syndergaard, S., and Hunt, D.: Estimates of the precision of

441    GPS radio occultations from the COSMIC/FORMOSAT-3 mission, Geophysical Research Letters, 34,

442    doi:10.1029/2006gl027557, 2007.

443    Schreiner, W., Sokolovskiy, S., Hunt, D., Rocken, C., and Kuo, Y. H.: Analysis of GPS radio occultation

444    data from the FORMOSAT-3/COSMIC and Metop/GRAS missions at CDAAC, Atmospheric

445    Measurement Techniques, 4, 2255-2272, doi:10.5194/amt-4-2255-2011, 2011.

446    Vorob'ev, V. V. and Krasil'nikova, T. G.: Estimation of the accuracy of the atmospheric refractive index

447    recovery from Doppler shift measurements at frequencies used in the NAVSTAR system, USSR,

448    Atmospheric and Oceanic Physics, English Translation, 29, 602-609, 1994.

449    Wickert, J., Marquardt, C., Beyerle, G., Reigber, C., and König, R.: Atmosphere sounding by GPS radio

450    occultation: First results from CHAMP, Geophysical Research Letters, 28, 3263-3266.

451    doi.org/10.1029/2001gl013117, 2001.

452    Wu, D. L.: Sporadic E morphology from GPS-CHAMP radio occultation, Journal of Geophysical

453    Research, doi:10.1029/2004ja010701, 2005.

454    Wu, D. L.: Ionospheric S4 Scintillations from GNSS Radio Occultation (RO) at Slant Path, Remote

455    Sensing, 12, doi:10.3390/rs12152373, 2020.

456     Yue, X., Schreiner, W. S., Zeng, Z., Kuo, Y. H., and Xue, X.: Case study on complex sporadic E layers

457     observed by GPS radio occultations, Atmospheric Measurement Techniques, 8, 225-236,

458     doi:10.5194/amt-8-225-2015, 2015.

459     Yue, X., Schreiner, W. S., Pedatella, N. M., and Kuo, Y. H.: Characterizing GPS radio occultation loss of

460     lock due to ionospheric weather, Space Weather, 14, 285-299, doi:10.1002/2015sw001340, 2016.

461     Zeng, Z. and Sokolovskiy, S.: Effect of sporadic E clouds on GPS radio occultation signals, Geophysical

462     Research Letters, 37, doi:10.1029/2010gl044561, 2010.

463

464
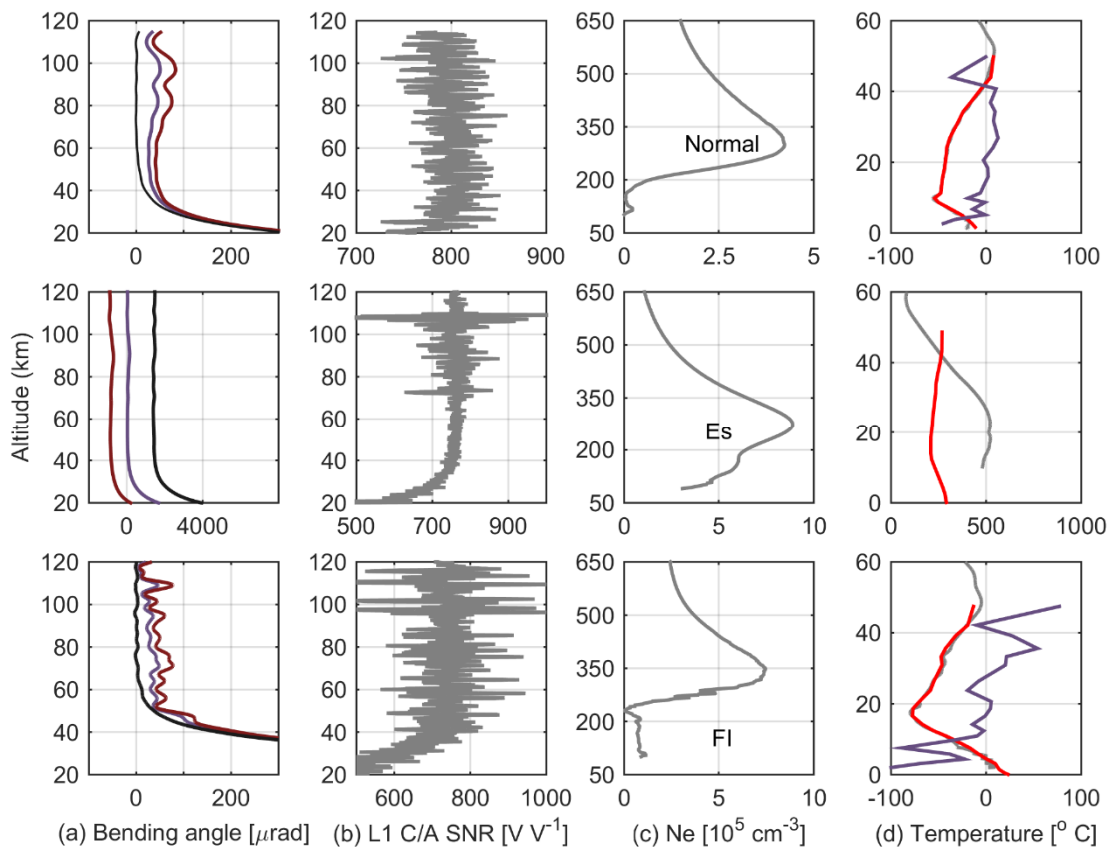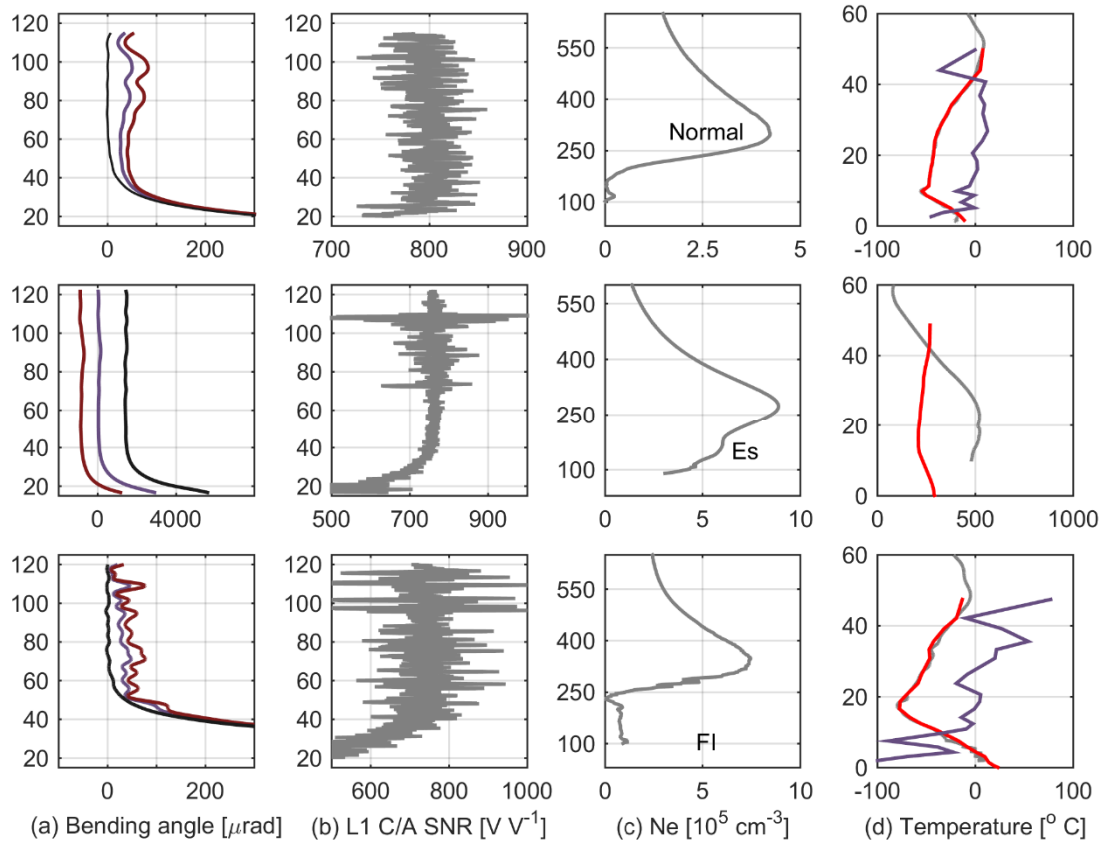
465 **Figure 1. Example of three cases occurred in 2013 made by COSMIC. Panels from top to bottom**

466    are normal example without the ionospheric irregularity occurrence, the Es example, and the F

467    region irregularity example. Panels from left to right are the inverted L1 (purple line), L2 (brown

468    line), and LC (black line) bending angles; the L1 C/A SNR, the electron density profile at the RO

469    tangent points; the inverted dry temperature (grey line) versus the ECMWF results (red line) as

470    well as their bias multiplied by 10 (purple line). Please note that the Y-axis of all panels represents

471    the altitude with kilometer (km) as the unit.
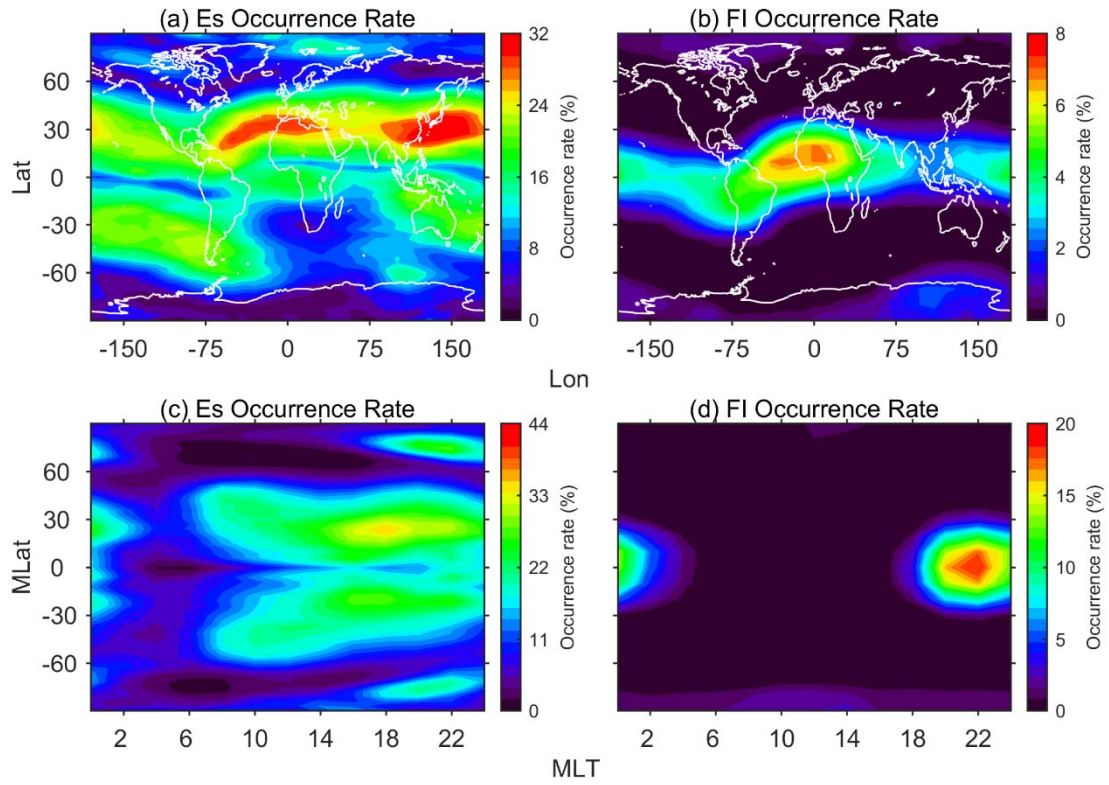
**Figure 2. Global geographical (top panels) and geomagnetic distributions (bottom panels) of the Es (left panels) and F layer irregularity occurrence rate (right panels), during 2011-2013.**
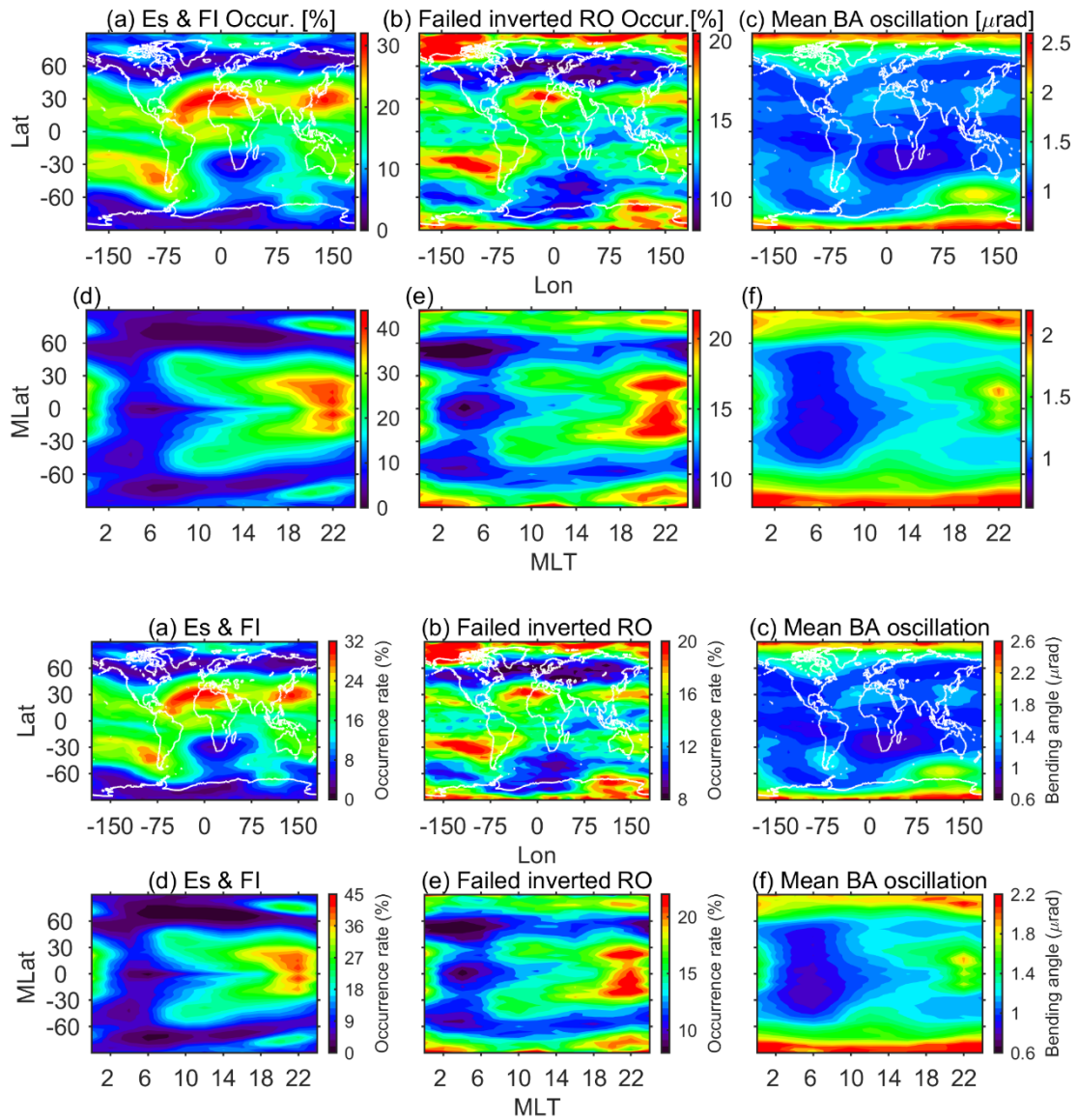
**Figure 23. Global geographical (top panels) and geomagnetic distributions (bottom panels) of the Es and F layer irregularity occurrence rate (left panels), the failed inverted RO event occurrence rate (middle panels), and the mean bending angle oscillation (right panels) during 2011-2013.**
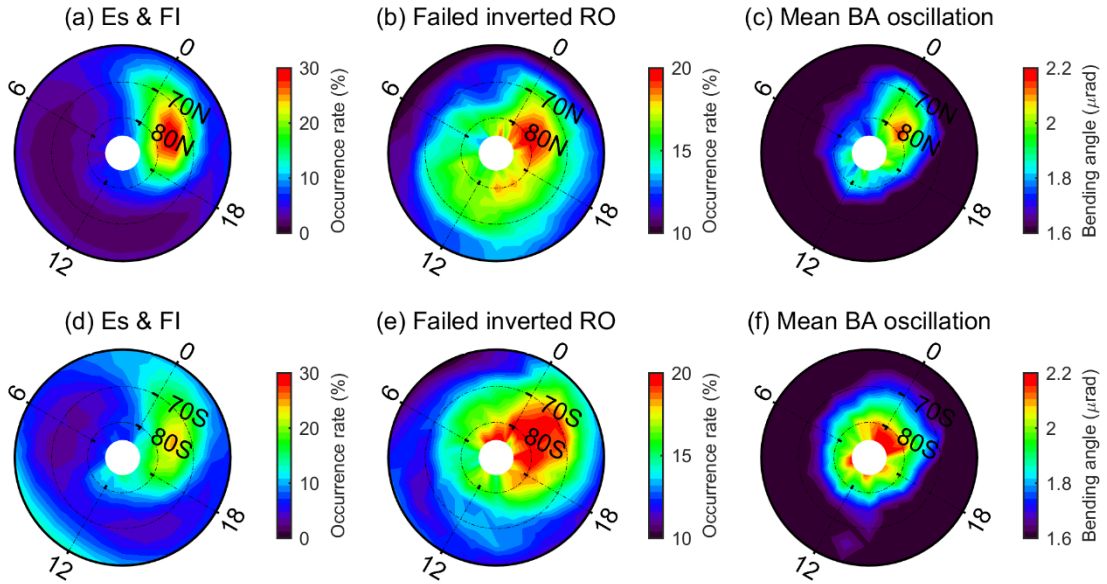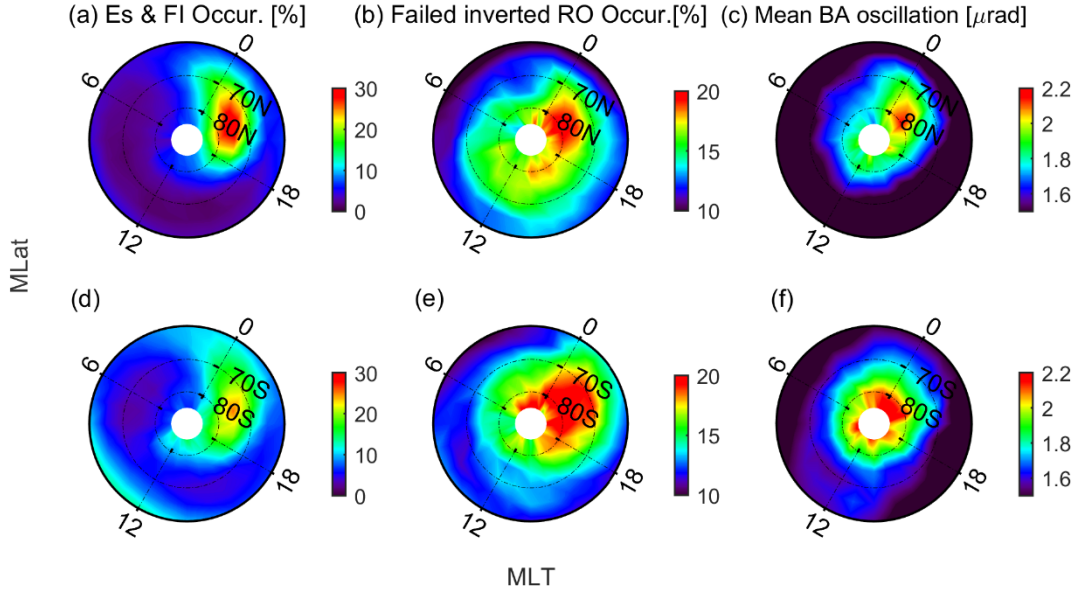
**Figure 34. MLT-MLat variation of the Es and F layer irregularity occurrence rate (left panels), the failed inverted RO occurrence rate (middle panels), and the mean bending angle oscillation (right panels) in polar regions. Please note that the top panels represent the results in northern polar regions while the bottom panels denote the southern polar regions.**
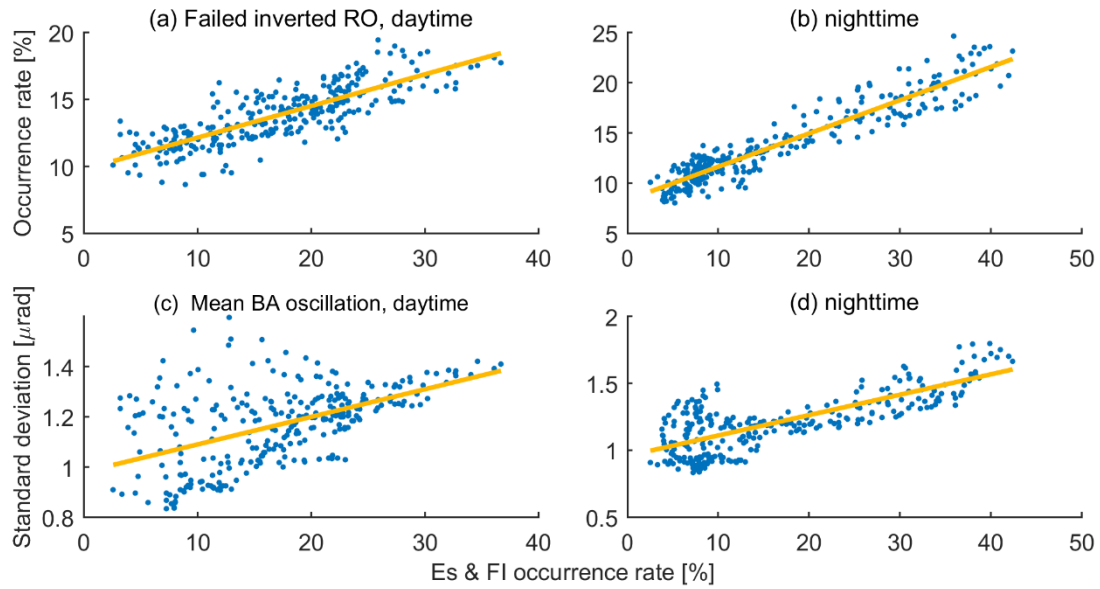
488

**Figure 45. Correlations between the ionospheric irregularity and the two parameters in middle and low latitudes (60° S-60° N) during the daytime (6~18 MLT, left panels) and nighttime (0~6 & 18~24 MLT, right panels) of 2011-2013. The yellow line is the corresponding linear least square fitting results.**
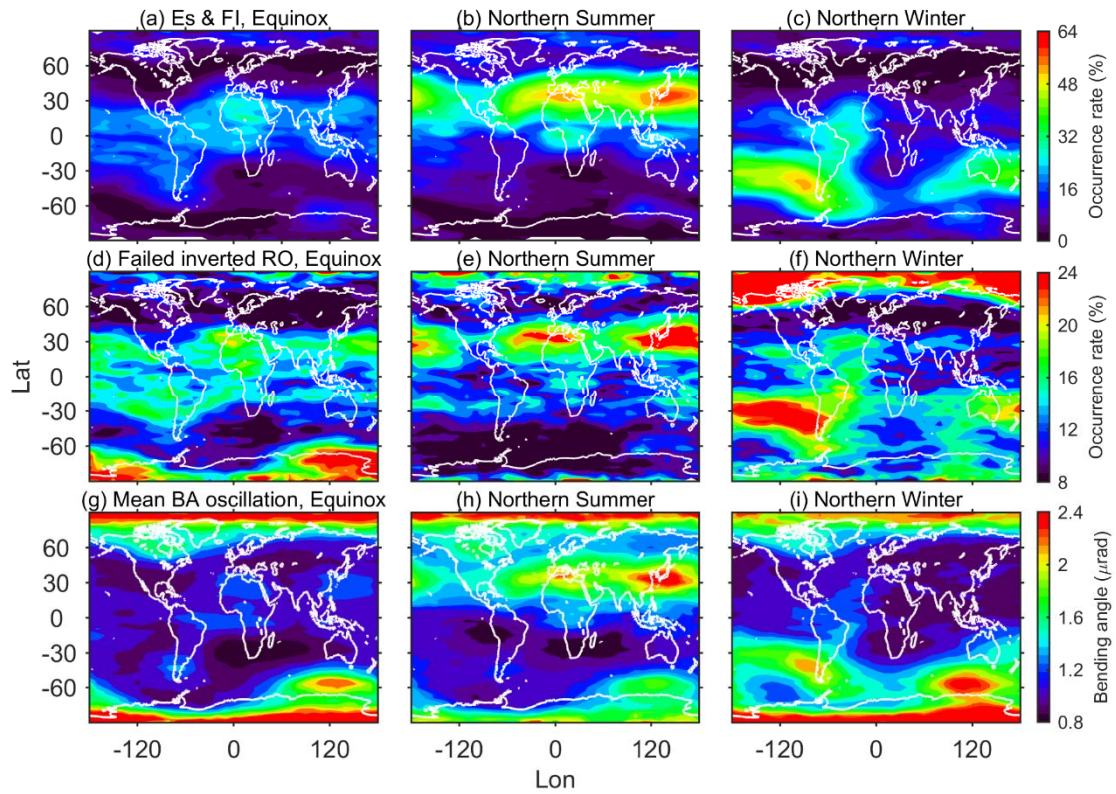
**Figure 56. Global geographical distribution of the Es and F layer irregularity occurrence rate (top panels), the failed inverted RO occurrence rate (middle panels), and the mean bending angle oscillation (bottom panels) for Equinox (left panels), Northern Summer (middle panels), and Northern Winter (right panels).**
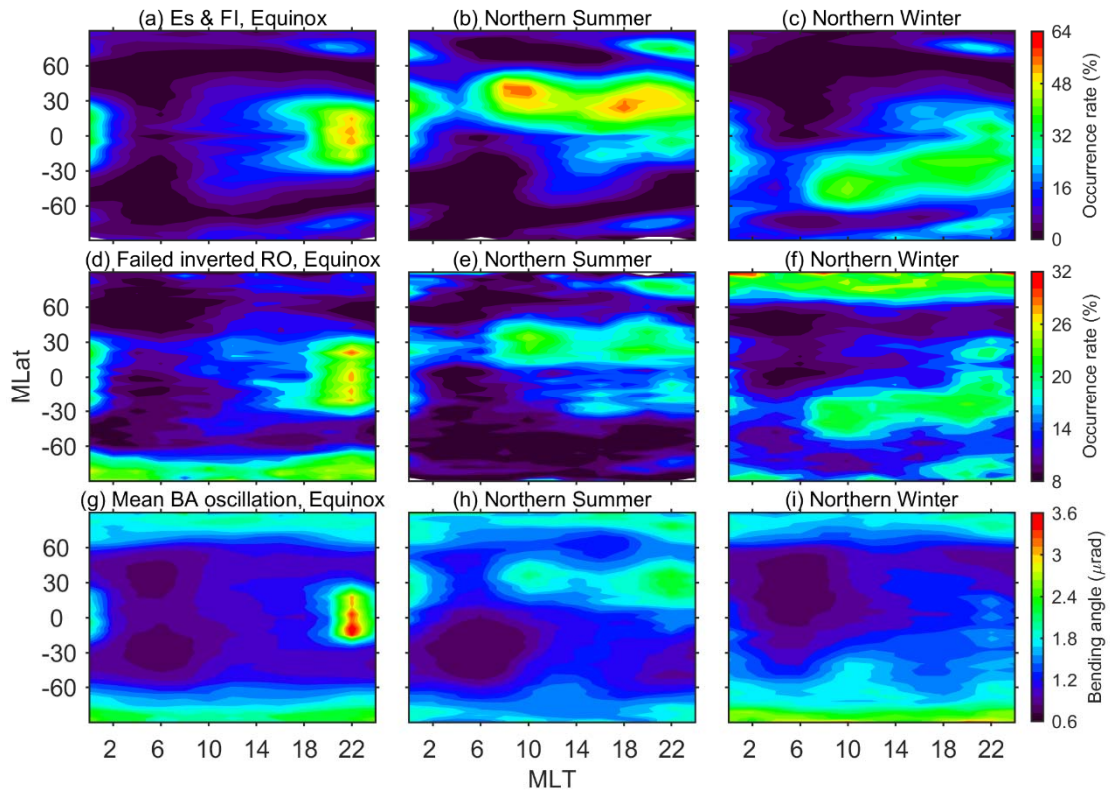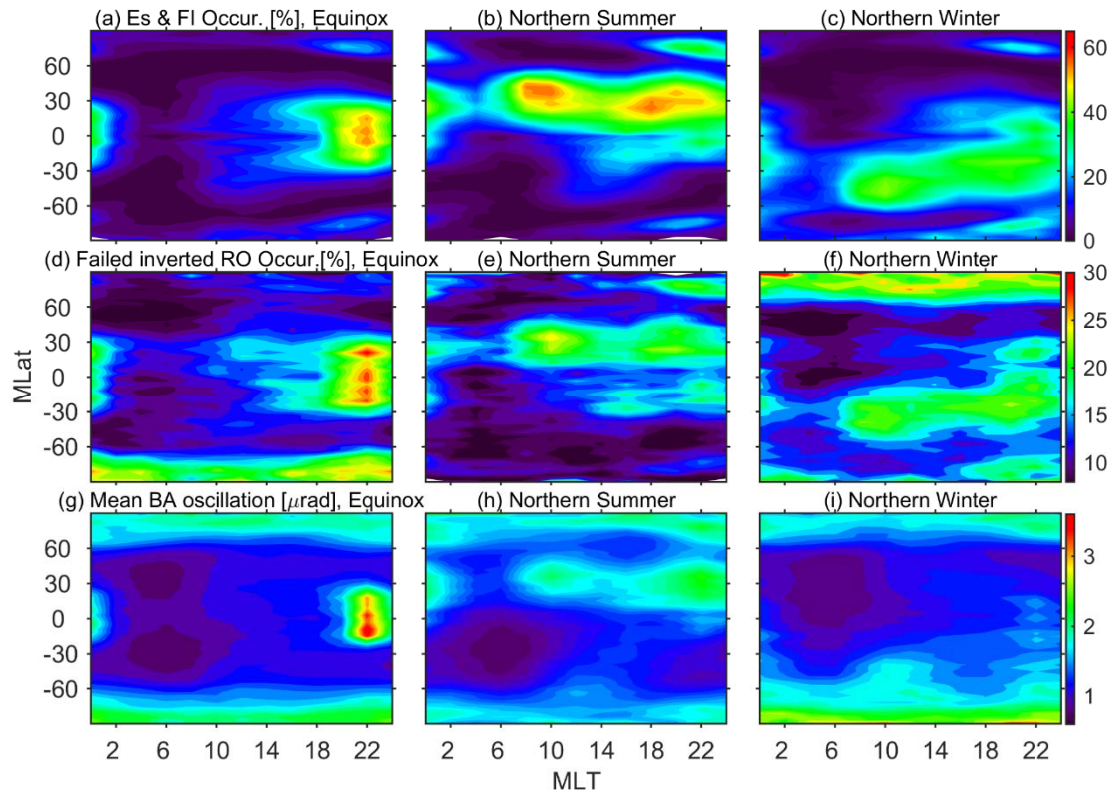
**Figure 6.7** The same as Figure 56, but for geomagnetic local time (MLT) and geomagnetic latitude (MLat) variation.